

The effects of the target material properties and layering on the crater chronology: the case of Raditladi and Rachmaninoff basins on Mercury

S. Marchi^{a,*}, M. Massironi^b, G. Cremonese^c, E. Martellato^d, L. Giacomini^b, L. Prockter^e

^a*Departement Cassiopée, Université de Nice - Sophia Antipolis, Observatoire de la Côte d'Azur, CNRS, Nice, France*

^b*Department of Geosciences, Padova University, Italy*

^c*INAF-Padova, Italy*

^d*Center of Studies and Activities for Space, Padova University, Italy*

^e*Applied Physics Laboratory, Johns Hopkins University, USA*

Abstract

In this paper we present a crater age determination of several terrains associated with the Raditladi and Rachmaninoff basins. These basins were discovered during the first and third MESSENGER flybys of Mercury, respectively. One of the most interesting features of both basins is their relatively fresh appearance. The young age of both basins is confirmed by our analysis on the basis of age determination via crater chronology. The derived Rachmaninoff and Raditladi basin model ages are about 3.6 Ga and 1.1 Ga, respectively. Moreover, we also constrain the age of the smooth plains within the basins' floors. This analysis shows that Mercury had volcanic activity until recent time, possibly to about 1 Ga or less. We find that some of the crater size-frequency distributions investigated suggest the presence of a layered target. Therefore, within this work we address the importance of considering terrain parameters, as geo-mechanical properties and layering, into the process of age determination. We also comment on the likelihood of the availability of impactors able to form basins with the sizes of Rachmaninoff and Raditladi in relatively recent times.

Keywords: Mercury, Raditladi basin, Rachmaninoff basin, Craters, Age determination

1. Introduction

During MESSENGER's third flyby of Mercury, a 290-km-diameter peak-ring (double-ring) impact basin, centered at 27.6° N, 57.6° E, was discovered and subsequently named Rachmaninoff. In terms of size and morphology, the Rachmaninoff basin closely resembles the 265-km-diameter Raditladi peak-ring basin, located at 27° N, 119° E west of the Caloris basin, that was discovered during MESSENGER's first flyby [24]. The image-mosaic of Rachmaninoff and its ejecta has a spatial resolution of 500 m/pixel and it is derived from images obtained by MESSENGER's Mercury Dual Imaging System (MDIS) narrow-angle camera [8], while Raditladi

*Corresponding author

Email address: marchi@oca.eu (S. Marchi)

basin and surrounding areas were imaged at 280 m/pixel. Both basins and surrounding areas were also imaged with a set of 11 filters of the MDIS wide-angle camera (WAC), whose wavelengths range from 430 to 1020 nm [8]. These images were used to obtain color maps with a resolution of about 5 km/pixel and 2.4 km/pixel for Rachmaninoff and Raditladi, respectively. The two basins appeared to be remarkably young because of the small number of impact craters seen within their rims [31, 24, 25]. For this reason it has been argued that they were likely formed well after the end of the late heavy bombardment of the inner Solar System at about 3.8 Ga [31]. In particular, for Raditladi it has been pointed out that the basin could be as young as 1 Ga or less [31, 25].

Interestingly, both basin floors are partially covered by smooth plains. In the case of Rachmaninoff, an inner floor filled with spectrally distinct smooth plains has been observed and this, combined with the small number of overimposed craters, implies a volcanic origin [25]. The estimate of the temporal extent of the volcanic activity and, in particular, the timing of the most recent activity may represent a key element in our understanding of the global thermal evolution of Mercury, and helps to constrain the duration of the geologic activity on the planet in light of the new data provided by MESSENGER. Moreover, Raditladi may be the youngest impact basin discovered on Mercury so far, and therefore it is important to understanding the recent impact history of the planet.

For all these reasons, the age determination of Rachmaninoff and Raditladi basins and their geologically different terrains is of a great interest. In this paper, we will present a revised Mercury crater chronology, and show how to take into account for the crustal properties of the target (§ 3). This chronology will be then applied to Rachmaninoff and Raditladi basins (§ 4).

2. The Model Production Function chronology

In this paper we date the Raditladi and Rachmaninoff basin units by means of the the Model Production Function (MPF) chronology of Mercury [16, 17]. This chronology relies on the knowledge of the impactor flux on Mercury and on the computed ratio of impactors between Mercury and the Moon. The absolute age calibration is provided by the Apollo sample radiometric ages. The crater scaling law enables computation of the crater size-frequency distribution (SFD) using a combination of the impactor SFD and the inferred physical properties of the target. The computed crater SFD per unit surface and unit time is the so-called MPF. The present model involves several improvements with respect to the model presented in [16] and [17], thus it will be described in detail in the next sections.

2.1. *The impactor SFD and the crater scaling law*

In the following analysis, we use the present Near-Earth Object (NEO) population as the prime source of impactors. This assumption is justified by the presumably young ages (i.e. low crater density) of the terrains studied in this paper. In particular, we use the NEO SFD as modeled by [2, 3]. This NEO SFD is in good agreement with the observed NEO population, fireballs and bolide events [see 16, for further details].

Concerning the crater scaling law, we adopted the so-called Pi-scaling law in the formulation by [12]. Unlike previous approaches, our methodology explicitly takes into account the crustal properties of the target. In fact, surfaces react differently to impact processes, depending on the bulk density, strength and bulk structure of the target material. These latter parameters are

taken into account by the scaling law, and are tabulated for several materials like cohesive soils, hard-rock and porous materials [e.g. 20, 12]. On a planetary body, terrain properties may vary from place to place according to the local geological history and as a function of the depth in the target crust. Therefore, impacts of different sizes taking place on a particular terrain may require different estimates of the target properties.

The Pi-scaling law allows computation of the transient crater diameter (D_t) as a function of impact conditions and target properties, and reads:

$$D_t = kd \left[\frac{gd}{2v_\perp^2} \left(\frac{\rho}{\delta} \right)^{\frac{2\nu}{\mu}} + \left(\frac{Y}{\rho v_\perp^2} \right)^{\frac{2+\mu}{2}} \left(\frac{\rho}{\delta} \right)^{\frac{\nu(2+\mu)}{\mu}} \right]^{-\frac{\mu}{2+\mu}} \quad (1)$$

where g is the target gravitational acceleration, v_\perp is the perpendicular component of the impactor velocity, δ is the projectile density, ρ and Y are the density and tensile strength of the target, k and μ depend on the cohesion of the target material and ν on its porosity¹. Therefore, the nature of the terrain affects the crater efficiency and the functional dependence of the crater size with respect to the input parameters (e.g. impactor size and velocity). Equation 1 accounts both for the strength and gravity regimes, allowing a smooth transition between the two regimes. The impactor size (d_{sg}) for which we have the transition between the two regimes is determined by equating the two additive terms in equ. 1, therefore:

$$d_{sg} = 2 \frac{v_\perp^2}{g} \left(\frac{Y}{\rho v_\perp^2} \right)^{\frac{2+\mu}{2}} \left(\frac{\rho}{\delta} \right)^\nu \quad (2)$$

The transient crater diameter is converted into final crater diameter (D) according to the following expressions:

$$D = 1.3D_t \quad \text{if } D_t \leq D_\star/1.3 \quad (3)$$

$$D = 1.4 \frac{D_t^{1.18}}{D_\star^{0.18}} \quad \text{if } D_t > D_\star/1.3 \quad (4)$$

where D_\star is the observed simple-to-complex transition crater diameter, which for Mercury is 11 km [23]. The conversion between transient crater to final crater is rather uncertain and several estimates are available [e.g. 11, 19, 7]. Here we have used the factor 1.3 from transient to final simple craters². For the complex craters, we use the expression proposed by [7], where the constant factor has been set to 1.40 in order to have continuity with the simple crater regime ($1.4 = 1.3^{1.18}$). We note that the effects of the material parameters on the transient crater size depend on whether a crater is formed in the strength or gravity regime. For the strength regime, $D \propto \rho^{-0.1}$ or $\propto \rho^{-0.2}$, while $D \propto Y^{-0.2}$ or $\propto Y^{-0.3}$ according to the values for μ and ν given above. In the gravity regime, $D \propto \rho^{-0.3}$. In all cases, the dependence of D on both ρ and Y is mitigated by the low exponents.

¹The values used are: $k = 1.03$ and $\mu = 0.41$ for cohesive soils, while $k = 0.93$ and $\mu = 0.55$ for rocks. ν has been set to 0.4 in all cases [12].

²The factor has been retrieved at <http://keith.aa.washington.edu/craterdata/scaling/theory.pdf> on January 2011.

2.2. Inhomogeneities of the target material parameters

The application of the crater scaling law is not straightforward, since the physical parameters of the terrains are poorly constrained for Mercury and the crater scaling law has been derived for idealized uniform target properties. So far, no detailed and systematic study has been performed to develop a crater scaling law for a layered target [e.g. 20, 5], although numerical modeling of terrestrial craters has shown that the target layering plays an important role in the cratering process [e.g. 6, and references therein]. On the other hand, we think that it is worth attempting to simulate a more realistic situation instead of using the same average values for craters whose sizes can vary by order of magnitudes and consequently involved different layers of a planetary crust. In this context, geological analysis of the terrains can provide valuable information, at least to constrain the surface properties of the target.

In this work, we assumed that the density and strength of Mercury varies as a function of the depth, in analogy to that inferred for the Moon [16, and references therein]. In figure 1 (left panels) the assumed density and strength profiles are indicated. These profiles are consistent with the upper lunar structure [13], and were adopted also for Mercury. In particular, we have considered a more or less fractured upper crust on top of a bulk silicic lower crust which in turn overlays a peridotitic mantle. However, it must be emphasized that the depths at which these layers occur may vary from place to place (see § 3).

For each impactor size, we have assigned average values for the target density and strength. Over a wide range of parameters, the transient crater radius (R_t) is about 10 – 20 times larger than the impactor radius r and the depth of the crater is typically between one-fourth and one-third of the crater size [20]. Thus the thickness of the excavated material is roughly between 2.5 – 7 impactor radii. Here we have adopted an intermediate value, namely averaging the density and strength up to a depth of $5r$ (see fig. 1, right panels) Given the limited variation in the density and strength profile, the choice of the actual depth to average the density and strength for a given impactor radius has a low influence ($< 5\%$) on the scaling law.

In addition to the density and strength profiles, we also consider a transition of the crater scaling law (from cohesive-soil to hard-rock) according to the size of the impactor. In fact, the density and strength profiles shown in fig. 1 describe a material of increasing coherence for increasing depth. This is the result of the continuous bombardment of planetary surfaces that produces comminution and fracturing of the upper crustal layers gradually decreasing with depth as observed in seismic profiles of the lunar crust underneath the Mare Cognitum [32, 28, 14]. In this respect, craters that affect only the upper fractured layers form in the cohesive-soil regime, while larger ones in hard-rock regime. Therefore the depth of the transition (H) from the superficial fractured layer to the unfractured lower crust is an important parameter. The depth (and therefore the crater size) at which the transition from one regime to the other occurs can vary from place to place. For instance, the thickness of the cohesive layer may be only of a few meters on recent lunar mare material [26], while it is expected to be of several kilometers on the highlands³. In the examples of fig. 1, it is assumed that $H = 10$ km [13].

The details of the transition are not easy to model. A simplified study of impact processes on a layered target was performed by [26]. They simulated a two-layer structure, formed by a loose, granular layer on top a more competent material. It was observed that the craters had the usual shapes for diameters less than about 4 times of the top layer thickness. Larger craters developed central mounds, flat floors and concentric rims indicating the presence of the underlying

³Note that, in principle, the above scenario maybe locally reversed, e.g. in the presence of fresh solidified lava on top of an older fractured layer.

layer. According to these results, we simplify the problem by considering a sharp transition in the crater scaling law, at $D_t = 4H$. This implies a transition as a function of impactor radius at $r = H/5 - H/10$. The effect of the transition in the scaling law is reported in fig. 2 for two depths of transitions. Note that the position of the sharp transition varies according to the depth assumed. In this paper, we use an intermediate value and set the transition at $r = H/7.5$. In a more realistic situation, a gradual transition should be predicted given that the target gradually changes its properties as function of the depth. Therefore, our simplified model is not expected to be accurate close to the transition region, nevertheless we believe it provides a reasonable way to approach the cratering scaling law for a layered target.

2.3. Deriving the Model Production Function

The NEO population and the crater scaling described in the previous section are used to derive the MPF per unit time (see fig. 3). The main outcome of our model is that the adopted transition in the crater scaling law results into a “S-shaped” feature (or flexure) in the MPF. The position of such feature, which is determined by H , is not known a-priori. However, as discussed in [17], in some cases H can be constrained by the shape of the observed crater SFD. Furthermore, the geological analysis of the terrains can help to derive the expected range of variation for H . For instance, lava emplacements may partly strengthen or even completely replace the pre-existing fractured layer. Hence in this latter cases the fractured horizon can be confined within a very thin regolith cover, negligible for our calculation ($H \sim 0$). For young units with poor crater statistics, the choice of H may affect the age determinations by up to a factor of 3-4. Thus, in order to derive a more accurate age estimate, it is of paramount importance to adapt the crater production function to the nature of the terrains investigated.

The absolute age is given by the lunar chronology, which expresses the lunar crater cumulative number at 1 km (N_1) as a function of time (t), using the following equation:

$$N_1(t) = a(e^{bt} - 1) + ct \quad (5)$$

where $a = 1.23 \times 10^{-15}$, $b = 7.85$, $c = 1.30 \times 10^{-3}$ [16]. The MPF function at a time t is given by:

$$\text{MPF}(t) = \text{MPF}(1\text{yr}) \cdot \frac{N_1(t)}{N_1(1\text{yr})} \quad (6)$$

The $\text{MPF}(t)$ is used to derive the model cratering age by a best fit procedure that minimizes the reduced chi squared value, χ_r^2 . Data points are weighted according to their measurement errors. The formal errors on the best age correspond to a 50% increase of the χ_r^2 around the minimum value.

It must be realized that the formal statistical error on the model age only reflects the quality of the crater SFDs. On top of that, other sources of uncertainties are present. They stem from the uncertainties involved in the physical parameters used in the model, although we want to stress here that the model ages are not very sensitive to details of the density and strength profile [see § 3.1 of 16]. A more important issue is the applicability of the present NEO population in the past. The $N_1(t)$ chronology function assumes a linear dependence with time in the last ~ 3.8 Ga, corresponding to an impactor population in a steady state. On the other hand, dynamical studies of recent main belt asteroid family formation suggested that the present NEO flux may be higher than the average steady flux by a factor of 2 [4]. This result also agrees to what found by

cratering studies of young lunar terrains [< 0.8 Ga; e.g. 16]. Concerning the layering structure, as described above, the choice of H might affect the age estimate by a factor of 3-4 at most. The uncertainty due to the layering is, nevertheless, typically present only for young terrains where the crater SFD has a limited range of crater dimensions. The layering affects the specific shape of the crater SFD, and has to be evaluated case by case, as it will be discussed in detail in the following sections. Finally, it must be noted that wavy features in the crater SFD can be due also to other processes than layering, like for instance partial crater obliteration due to subsequent lava flows. Therefore, the nature of the S-shaped feature must be constrained as much as possible by geological analysis in order to achieve a more reliable age determination.

3. Geological analysis and model ages

Geological maps of the Rachmaninoff and Raditladi basins were constructed considering both floors and ejecta. For the floor terrains, the geological units were identified on the base of their different surface morphologies and spectral characteristics (i.e., albedo), along with an analysis of their stratigraphic relationships. The ejecta units, surrounding the basins, were outlined considering exclusively the area of continuous ejecta blankets, which are easily detectable thanks to their characteristic hummocky surface. The geological maps also take into account tectonic features affecting the areas.

Crater age determination is based on the primary craters, i.e. those formed by impacts with objects in heliocentric orbits. Hence, a crucial point in assessing age by crater counts is to identify and avoid secondary craters. Most of the secondaries are recognizable because they are directly related to their primaries (e.g., the secondaries are arranged in radial patterns around the primary), or occur in loops, cluster and chains. The contribution of far-field secondaries, which are normally not distinguishable from primary craters [e.g. 18], has been neglected. Although this is a reasonable assumption for Rachmaninoff and Raditladi basins given their low crater densities and thus their presumable relatively young ages, MPF model ages may overestimate real ages.

3.1. *Rachmaninoff basin*

The Rachmaninoff basin is surrounded by a continuous ejecta blanket and includes an interior peak ring structure, about 136 km in diameter, with extended smooth plains filling its floor. Most of the basin walls are modified into terraces. Several different geological units have been distinguished inside the floor on the basis of their different relative albedo and surface texture (fig. 4). The inner smooth plains are mostly within the peak ring except in the southern quadrant of Rachmaninoff, where the smooth plains cover or embay the peak ring structure and some of the annular units within the rim. This observation suggests an origin of volcanic emplacement. In the WAC enhanced-color images these plains show a yellow to reddish tone which stands out from the darker and bluer color of the other units within the basin and surrounding regions [25]. This clearly supports a different composition and origin of these inner smooth plains. Several discontinuous and concentric troughs possibly due to the uplift and extension of the basin floor, affect the area enclosed by the peak ring [25] and have been interpreted to be graben. The annular region between the peak ring and the rim basin includes seven different units. The most prominent is made up of bright materials, apparently younger than all the other units and possibly related to explosive volcanism [25]. Peak ring and terrace material boundaries stand out for their relief, whereas hummocky, dark, irregular and annular smooth plains do not show unequivocal

Table 1: Statistics of all the features detected on Rachmaninoff and Raditladi basin floors and ejecta. “All” indicates all crater-like features, “Bon” the bonafide craters, “Sec” secondary craters (which includes chain, cluster and elliptical craters), “End” endogenic (volcanic and tectonic) features. “Inn. pl.” and “Ann. un.” stand for inner plain and annular unit, respectively.

Count	Rach			Rad		
	Inn. pl.	Ann. un.	Ejecta	Inn. pl.	Ann. un.	Ejecta
All	37	119	1154	231	214	1518
Bon	13	51	180	79	96	452
Sec	1	46	974	34	91	1029
End	23	22	0	118	27	37

stratigraphic relationships with each other [25]. This suggests an almost coeval origin of these units that may consist of impact melts and breccias. This is furthermore confirmed by the WAC images, where annular units do not reveal any color variations and are characterized by uniform blue color similar to the surrounding terrain. To shed more light on the origin of the floor material we dated the Rachmaninoff basin using crater statistics of annular units and inner plains separately. Bright material was neglected in the crater counts due to its limited extent. Craters in the ejecta blanket were counted as well (fig. 4).

Easily recognizable secondary craters (either elliptical in shape or arranged in loops and chains) have not been detected within the Rachmaninoff inner plains but numerous pits up to 3.5 km in diameter have been found in close proximity to the concentric grabens. These features are very unlikely to be impact craters and in our interpretation are most probably of tectonic (structural pits, fault bounded depressions, en-echelon structures) and/or volcanic (more or less irregular vents) origin (fig. 5, panels A and B). For this reason their counts were neglected for the purposes of age determination. Clusters and chains of secondaries with irregular and elliptical shapes were recognized in the western sector of the annular units and appear to be directly related to a nearby 60 km primary peak crater overlying the Rachmaninoff ejecta (fig. 5, panels C and D). Self secondaries are numerous within the ejecta blanket.

The resulting crater count statistics are reported in Table 1 where for each terrain, all crater-like features, bonafide craters, secondary craters and endogenic (namely volcanic or tectonic) features are listed. It is interesting to compare the SFDs of all the counts (fig. 6). According to our best interpretation of the detected features, the inner plains contain more endogenic features than bonafide craters. Hence, in our opinion the uneven distribution in R plots of crater-like features smaller than 4 km, which is generally attributed to the effect of far field secondaries on Mercury [31], are in this case dominated by tectonic and volcanic features. For the annular units, both the secondary crater and endogenic SFDs have steeper slopes with respect to the bonafide crater SFD, moreover they are limited to features smaller than 4-5 km. Hence, for the annular units as well as the inner plains, the identification of endogenic features is clearly very important since it heavily affects the final bonafide crater SFD. On the ejecta, most of the crater-like features appear to be self secondaries mostly arranged into clusters and chains and/or with an elliptical shape. All the terrains were dated using their bonafide crater SFDs.

The MPF fits of the observed crater SFDs are shown in figure 7. The lower panel shows the distribution of bonafide primary impact craters detected on the ejecta blanket. A remarkable feature in the crater SFD of the ejecta is the presence of a flexure point at about $D = 15$ km. The actual shape of the bonafide crater SFD is partially due to the feature selection. Nevertheless, we think that at the large crater sizes relevant here, our selection is reliable and, consequently, the

observed flexure point is likely a real feature possibly reflecting a layered target with an upper weak horizon. Hence the MPF best fit is achieved with $H = 3$ km and gives a model age of 3.54 ± 0.1 Ga.

In fig. 7 (upper panel) the bonafide crater SFD on inner plains and annular units are shown. Note that, unlike the ejecta, both cases do not show the presence of a flexure point. This may be due to a real absence of an upper weak horizon or to the lack of large craters that would have otherwise allowed to retrieve information on the geomechanical properties of the deep crustal layers. The annular units are composed of breccias more or less welded by impact melts which can have only partially strengthened the fractured material either pre-dating or originating from the Rachmaninoff impact. Hence, it is reasonable to assume at least the same H of the crust beneath the ejecta. This leads to a model age of 3.6 ± 0.1 Ga, which is consistent with the model age of the ejecta and likely dates the Rachmaninoff impact event.

The inner plains are characterized by much poorer statistics within a small range of diameters, therefore the crater SFD cannot be used to infer H . Nevertheless, geological analysis suggest that the inner plains are younger volcanic flows on the basis of their different albedo, color and overlapping relationship with respect to the unit emplaced between the peak-ring and the basin rim [25]. This would make possible also the scenario in which the former fractured horizon, either pre-dating or originating from the impact itself, was completely hardened by the rising magmas and emplacement of lava fields (fig. 8a). In this case, the MPF acceptably fits the bonafide crater size distribution giving a model age of 0.7 ± 0.2 Ga (fig. 7). By contrast the fit would be very poor if the all crater-like features would be taken into account. This is not surprising considering the strong contribution we infer that tectonic and volcanic features have on the inner plains statistics. Another possible scenario is that the magmatic activity within Rachmaninoff was unable to totally strengthen the upper weak layer comprising of fractured material originated by the impact itself or inherited by primordial events. This could be due to either weakly sustained volcanism, which emplaced a thin volcanic sequence on top of a fractured material, and/or, a magma influx concentrated along few well defined conduits within a still fractured crust underneath the basin (fig. 8b). In this case we also computed the model age using $H = 3$ km as for the annular units and ejecta, obtaining a value of 1.5 ± 0.4 Ga. In both cases (upper weak crustal layer absent or preserved) the inner plains turn out to be remarkably young, and demonstrate that a recent volcanic activity occurred within the basin.

3.2. Raditladi basin

Raditladi contains an interior peak-ring structure 125 km in diameter and its walls appear to be degraded, with terraces most pronounced within the north and west sides of the rim [24]. A continuous ejecta blanket with no visible system of rays surrounds the basin and extends up to 225 km from the basin rim (Fig. 9). The floor is partially filled with smooth, bright reddish plains material that clearly embays the rim and the central peak ring [1, 24]. The northern and southern sectors of the basin floor consist of dark, relatively blue hummocky plains material confined between the rim and the peak ring. Troughs are found close to the center of the basin arranged in a partially concentric pattern, ~ 70 km in diameter, and are interpreted either as graben resulting from post-impact uplift of the basin floor, or as circular dikes possibly representing fissural feeding vents [9, 25]. Floor material was subdivided into two different units following [24]: smooth and hummocky plains. Smooth plains may have a volcanic origin, as appears to be the case for plains in the nearby Caloris basin [9, 27], however no clear stratigraphic relation with the hummocky plains has been found, suggesting that all the different terrains within Raditladi basin

may be coeval and directly related to the impact [25]. With respect to the ejecta area, we have selected the hummocky continuous ejecta blanket surrounding the basin.

We performed a crater count of the inner plains within the peak ring and the annular units enclosed between the basin rim and the peak ring. Counts were also performed on the ejecta blankets.

Within the inner plains, numerous small graben-related pits up to 5 km in diameter are identified; as for the case of Rachmaninoff, they are most probably tectonically-originated features and/or volcanic vents (fig. 10, panels A and B). Specifically, two peculiar pits in the northern inner plains were interpreted as volcanic vents for the dark material on the crater floor [9]. Secondary craters have been found associated to a 23-km crater within the inner plains (fig. 10, panels A and C). Some secondaries are also present on the annular plains, whereas the ejecta blanket is characterized by numerous self secondary craters, occurring mainly in clusters and chains. Figure 9 shows the bonafide craters. The statistics of all the identified features are reported in table 1, whereas the corresponding SFDs are shown in fig. 11.

The cumulative bonafide crater SFDs for different terrains of the Raditladi basin are shown in fig. 12, along with the MPF model ages.

The measured crater SFD on the ejecta blanket shows a flexure at about $D = 2 - 3$ km. The position of the flexure is well above the size of craters that can no longer be distinguished because of the image resolution, nevertheless the contribution of secondary craters at these crater sizes might be important. In the assumption that this feature is due to the layering, the best fit achieved for $H = 0.4$ km gives a model age of 1.3 ± 0.1 Ga. The best fit for the annular units is achieved using $H = 0.7$ km and the resulting model age is 1.1 ± 0.1 Ga. These values are consistent with both the layering and model age inferred for the ejecta blankets. For this reason the basin formation can be reliably fixed at around 1.1-1.3 Ga in accordance with the age suggested by [31] on the basis of a relative-chronology approach. As for the Rachmaninoff basin, the poor statistics and the limited range of diameters imply that the inner plains SFD cannot be used to constrain H . We derived the model age with both the same H of the annular units ($H = 0.7$ km), and a negligible thickness ($H \sim 0$), obtaining 2.2 ± 0.3 Ga and 1.1 ± 0.1 Ga, respectively. The former model age leads to a paradox given that the annular units are certainly coeval with the basin formation and, consequently, must only be older or of the same age as the smooth plains. Hence, the most reliable result for the inner plains is to consider a solid material yielding a crater retention age of about 1.1 Ga. The solid material could be due to an emplacement of lavas soon afterward the impact leading to a complete hardening of the fractured and brecciated material within the basin (fig. 13a). This interpretation is consistent with the presence of volcano-tectonic features within the basin but may conflict with both the absence of distinctive color variations of the inner plains with respect to the surrounding areas and their unclear stratigraphic relationship with the annular units. Alternatively, a great amount of impact melts able to completely harden the impact breccias may explain the derived crater retention age (fig. 13b).

4. Discussion and conclusions

MPF crater chronology has been applied to date the Rachmaninoff and Raditladi basins. Age assesment has been performed taking into account target rheological layering and using the present NEO population as the prime source of impactors.

Our results demonstrate that the volcanic activity within the Rachmaninoff basin interior significantly post-dates the formation of the basin. The basin itself probably formed about 3.6 Ga ago, whereas the volcanic inner plains may have formed less than 1 Ga ago. Therefore, Mercury had

a prolonged volcanic activity, which possibly persisted even longer than on the Moon, where the youngest detected nearside flows [on Oceanus Procellarum; 10] are about 1.1 Ga old. On the other hand, the Raditladi basin has an estimated model age of about 1 Ga and no firm indication that the inner plains formed more recently than the basin itself. Hence, these plains may be due to either huge volumes of impact melts or lavas emplaced soon afterward the basin formation. In the latter case, which is not clearly supported by the stratigraphic observations, volcanism might have been triggered by the impact itself.

This work also shows the role of target properties in deriving the age of a surface. Where such properties are neglected, as in traditional chronologies [e.g. 22], the crater production function may be unable to accurately reproduce the observed crater SFD and/or to provide a consistent age for nearby terrains. The following examples serve to illustrate this point: the Rachmaninoff ejecta bonafide crater SFD shows an S-shaped feature that, according to our best knowledge, cannot be ascribed to processes other than a layered target; the Raditladi inner plains have an higher density of craters than the annular units, implying a paradoxically older age for the interior plains if the inner and outer plains had the same material properties.

The derived ranges of ages for Raditladi basin imply that its formation occurred long after the late heavy bombardment (~ 3.8 Ga), at a time when the primary source of impactors was a NEO-like population. This conclusion also likely applies to Rachmaninoff basin, even if it cannot be excluded that it was formed during or prior the late heavy bombardment. The NEOs average impact velocity on Mercury is about 42 km/s [15]. Considering a most probable impact angle of $\pi/4$, the projectiles responsible for Rachmaninoff and Raditladi formation should have had diameters in the range 14-16 km (see fig. 2). In the present NEO population, bodies are quickly replenished -in time scales of tens of Myrs- mainly from the main belt via slow orbital migration into major resonances. Such a migration, due mainly to Yarkowsky effect, is size dependent and is negligible for objects larger than ~ 10 km. Therefore larger objects, such as those required for the formation of the Raditladi and Rachmaninoff basins, are mainly produced by dynamical chaos loss [21]. Those simulations show that the rate of large impactors decreased by a factor of 3 over the last 3 Ga. Another source of large impactors is the sporadic direct injection into strong resonances due to collisions [34]. The present NEOs' average impact probability with Mercury in the size range of 14-16 km, is of about one impact every 3.3 Ga, in agreement with the proposed timescales of the formation of Rachmaninoff and Raditladi.

Acknowledges

The authors wish to thank P. Michel for helpful discussions on the cratering processes on a layered target. We also wish to thank A. Morbidelli for discussions regarding the NEO population. Finally, we thank the referees (C. Chapman and an anonymous one) for providing very interesting comments, that helped to improve our work.

References

- [1] Blewett D.T., Robinson M.S., Denevi B.W., Gillis-Davis J.J., Head J.W., Solomon S.C., Holsclaw G.M., McClintock W.E., 2009. Multispectral images of Mercury from the first MESSENGER flyby: Analysis of global and regional color trends. *Earth Planet. Sci. Lett.*, 285(3-4), 272-282.
- [2] Bottke, W. F., Jedicke, R., Morbidelli, A., Petit, J.-M., & Gladman, B. 2000. Understanding the Distribution of Near-Earth Asteroids. *Science*, 288, 2190-2194.
- [3] Bottke, W. F., Morbidelli, A., Jedicke, R., Petit, J.-M., Levison, H. F., Michel, P., & Metcalfe, T. S. 2002. Debiased Orbital and Absolute Magnitude Distribution of the Near-Earth Objects. *Icarus*, 156, 399-433.
- [4] Bottke, W. F., Vokrouhlický, D., & Nesvorný, D. 2007. An asteroid breakup 160 Myr ago as the probable source of the K/T impactor. *Nature*, 449, 48-53.
- [5] Collins, G. S., Melosh, H. J., & Marcus, R. A. 2005. Earth Impact Effects Program: A Web-based computer program for calculating the regional environmental consequences of a meteoroid impact on Earth. *Meteorit. Planet. Sci.*, 40, 817-840.
- [6] Collins, G. S., Kenkmann, T., Osinski, G. R., Wünnemann, K. 2008. Mid-sized complex crater formation in mixed crystalline-sedimentary targets: Insight from modeling and observation. *Meteorit. Planet. Sci.*, 43, 1955-1977.
- [7] Croft, S. K. 1985. The scaling of complex craters. *Proc. Lunar Planet. Sci. Conf.*, 15, 828-842.
- [8] Hawkins, S.E., Boldt, J.D., Darlington, E.H., Espiritu, R., Gold, R.E., Gotwols, B., Grey, M.P., Hash, C.D., Hayes, J.R., Jaskulek, S.E., Kardian, C.J., Keller, M.R., Malaret, E.R., Murchie, S.L., Murphy, P.K., Peacock, K., Prockter, L.M., Reiter, R.A., Robinson, M.S., Schaefer, E.D., Shelton, R.G., Sterner, R.E., Taylor, H.W., Watters, T.R., Williams, B.D., 2007. The Mercury Dual Imaging System on the MESSENGER Spacecraft. *Space Sci. Rev.*, 131, 247-338.
- [9] Head J.W., Murchie S.L., Prockter L.M., Solomon S.C., Strom R.G., Chapman C.R., Watters T.R., Blewett D.T., Gillis-Davis J.J., Fassett C.I., Dickson J.L., Hurwitz D.M., Ostrach L.R., 2009. Evidence for intrusive activity on Mercury from the first MESSENGER flyby. *Earth Planet. Sci. Lett.*, 285(3-4), 251-262.
- [10] Hiesinger, H., Head, J. W., III, Wolf, U., & Neukum, G. 2001. New Age Determinations of Lunar Mare Basalts in Mare Cognitum, Mare Nubium, Oceanus Procellarum, and Other Nearside Mare. *Lunar Planet. Inst. Sci. Conf. Abstracts*, 32, 1815.
- [11] Holsapple, K. A. 1993. The scaling of impact processes in planetary sciences. *Annu. Rev. Earth Planet. Sci.*, 21, 333-373.
- [12] Holsapple, K. A., Housen, K. R. 2007. A crater and its ejecta: An interpretation of Deep Impact. *Icarus*, 187, 345-356.
- [13] Hörz, F., Grieve, R., Heiken, G., Spudis, P., and Binder, A. 1991. Lunar surface processes. In *Lunar Sourcebook: A User's Guide to the Moon* (G. H. Heiken, D. T. Vaniman, and B. M. French, eds.) Cambridge University Press, Cambridge. 61-120.
- [14] Khan, A.K. Mosegaard, K.L. Rasmussen. 2000. A new seismic velocity model for the Moon from a Monte Carlo inversion of the Apollo lunar seismic data. *J. Geophys. Res. Lett.*, 27(11), 1591-1594.
- [15] Marchi, S., Morbidelli, A., Cremonese, G. 2005. Flux of meteoroid impacts on Mercury. *Astron. Astrophys.*, 431, 1123-1127.
- [16] Marchi, S., Mottola, S., Cremonese, G., Massironi, M., Martellato, E. 2009. A New Chronology for the Moon and Mercury. *Astron. J.*, 137, 4936-4948.
- [17] Massironi, M., Cremonese, G., Marchi, S., Martellato, E., Mottola, S., Wagner, R.J. 2009. Mercury chronology revisited through MPF application on Mariner 10 data: new geological implications. *J. Geophys. Res. Lett.*, 36, 21204.
- [18] McEwen, A. S., & Bierhaus, E. B. 2006. The Importance of Secondary Cratering to Age Constraints on Planetary Surfaces. *Annu. Rev. Earth Planet. Sci.*, 34, 535-567.
- [19] McKinnon, W. B., & Schenk, P. M. 1985. Ejecta Blanket Scaling on the Moon and - Inferences for Projectile Populations. *Lunar Planet. Inst. Sci. Conf. Abstract*, 16, 544.
- [20] Melosh, H. J., 1989. *Impact Cratering: A Geologic Process*. Oxford University Press, New York 1989, pp. 245.
- [21] Minton, D. A., & Malhotra, R. 2010. Dynamical erosion of the asteroid belt and implications for large impacts in the inner Solar System. *Icarus*, 207, 744-757.

- [22] Neukum, G., & Ivanov, B. A. 1994, Hazards Due to Comets and Asteroids, 359.
- [23] Pike, R. J. 1988. Geomorphology of impact craters on Mercury. Mercury (A89-43751 19-91). Tucson, AZ, University of Arizona Press, 1988, p. 165-273.
- [24] Prockter, L.M., Watters, T.R., Chapman, C.R., Denevi, B.W., Head, J.W., Solomon, S.C., Murchie, S.L., Barnouin-Jha, O.S., Robinson, M.S., Blewett, D.T., Gillis-Davis, J. 2009. The Curious Case of Raditladi Basin. Lunar Planet. Sci. Conf. Abstract, 40, 1758.
- [25] Prockter, L.M., Ernst, C.M., Denevi, B.W., Chapman, C.R., Head III, J.W., Fassett, C.I., Merline, W.J., Solomon, S.C., Watters, T.R., Blewett, D.T., Cremonese, G., Marchi, S., Massironi, M., Barnouin, O.S. 2010. Evidence for young volcanism on Mercury from the third MESSENGER flyby. Science, 329, 668-671.
- [26] Quaide, W. L., & Oberbeck, V. R. 1968. Thickness Determinations of the Lunar Surface Layer from Lunar Impact Craters. J. Geophys. Res., 73, 5247.
- [27] Robinson M.S., Murchie S.L., Blewett D.T., Domingue D.L., Hawkins S.E., Head J.W., Holsclaw G.M., McClinck W.E., McCoy T.J., McNutt R.L., Prockter L.M., Solomon S.C., Watters T.R. 2008. Reflectance and Color Variations on Mercury: Regolith Processes and Compositional Heterogeneity. Science, 321, 66-69.
- [28] Simmons G., Todd T., Wang H. 1973. The 25 km discontinuity: Implications for lunar history. Science, 182, 158-161.
- [29] Steffl, A. J., Cunningham, N. J., Durda, D. D., & Stern, S. A. 2009, AAS/Division for Planetary Sciences Meeting Abstracts, 41, #43.01
- [30] Stöffler, D., & Ryder, G. 2001. Stratigraphy and Isotope Ages of Lunar Geologic Units: Chronological Standard for the Inner Solar System. Space Sci. Rev., 96, 9-54.
- [31] Strom, R.G., Chapman, C.R., Merline, W.J., Solomon, S.C., Head, J.W. 2008. Mercury Cratering Record Viewed from MESSENGER's First Flyby. Science, 321, 79.
- [32] Tokosoz M.N., Press F., Dainty A., A., Anderson K., Latham G., Ewing M. Dorman J., Lammlein D., Sutton G., Duennebeir F. 1972. Structure composition and properties of lunar crust. Proc. Lunar Planet. Sci. Conf., 3, 2527-2544.
- [33] Wagner, R., Head, J. W., Wolf, U., & Neukum, G. 2002. Stratigraphic sequence and ages of volcanic units in the Gruithuisen region of the Moon. J. Geophys. Res., 107, 5104
- [34] Zappala, V., Cellino, A., di Martino, M., Migliorini, F., & Paolicchi, P. 1997. Maria's Family: Physical Structure and Possible Implications for the Origin of Giant NEAs. Icarus, 129, 1-20.

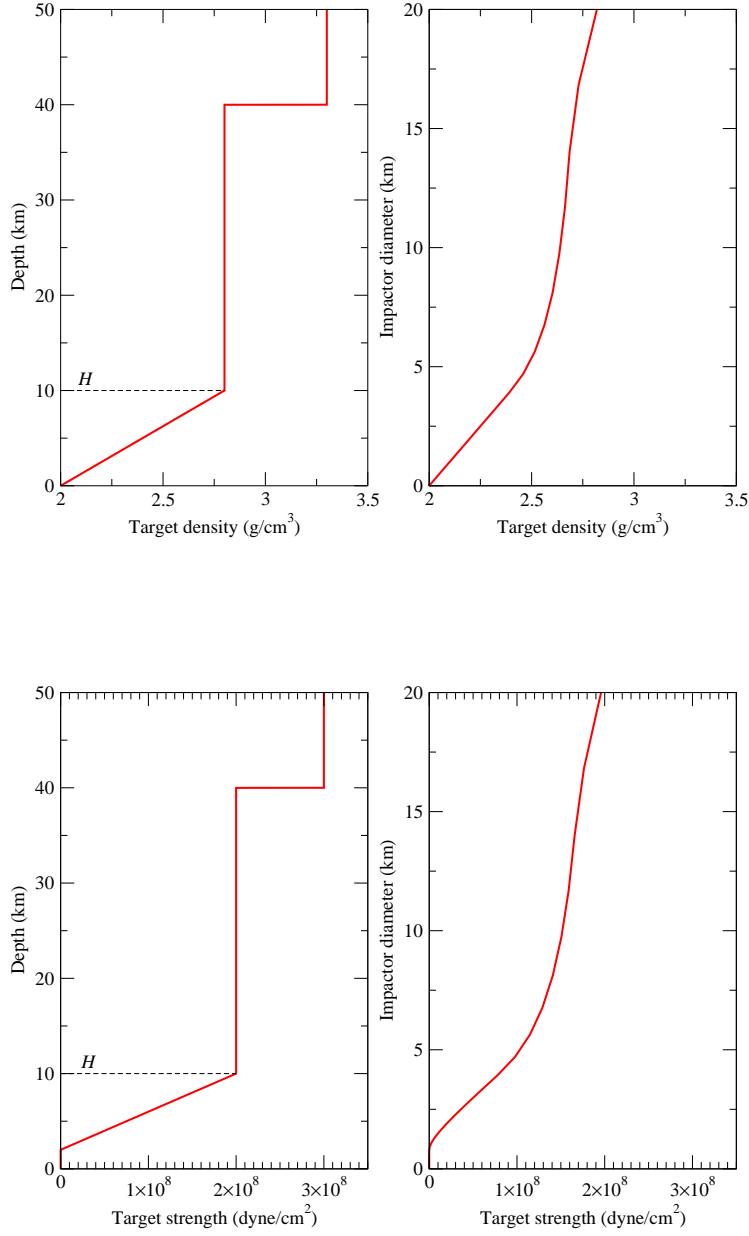


Figure 1: Inferred density and strength profiles for Mercury. Left panels report the assumed profiles as a function of depth. The discontinuous transitions correspond to the major transitions in the crust, in analogy to the lunar crust. The depth of the upper cohesive layer (H) is also indicated for clarity. In this example, it has been set to 10 km. The right panel shows the averaged density and strength as a function of the impactor diameter. This result has been achieved by averaging, for an impactor of radius r , both the density and strength up to a depth of $5r$ (see text).

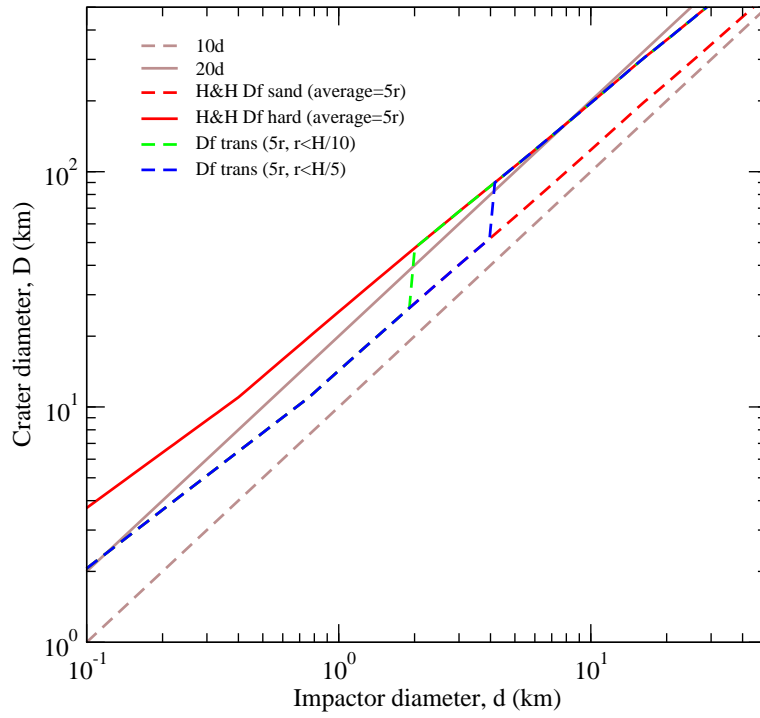


Figure 2: Crater scaling laws from Mercury. The plot reports the crater scaling laws for both cohesive material (dashed red line) and hard-rock material (solid red line). Two examples of the scaling law corresponding to the layered target are shown. They correspond to a transition in the crater scaling law for impactor radius $r = H/10$ (green dashed line) and $r = H/5$ (blue dashed line). These values correspond to the predicted uncertainties in the modeling of the transition (see text), and in the rest of the work we adopt an intermediate value of $r = H/7.5$. The depth of the cohesive layer H has been set to 10 km and density and strength are averaged to a depth of $5r$. In all cases, the curves are derived for the average impact velocity of 42 km/s, and an impact angle of $\pi/4$. The estimated impactor sizes that formed Rachmaninoff and Raditladi basins are also shown.

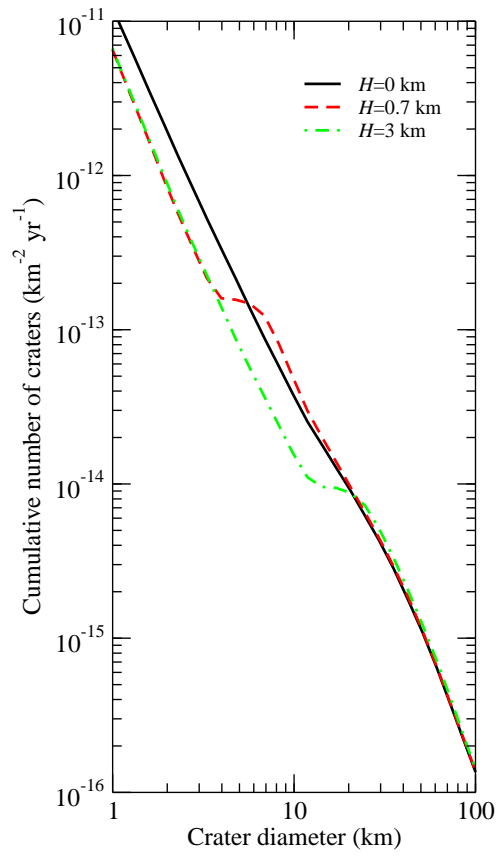


Figure 3: Examples of computed crater size-frequency distributions per unit surface per unit time (the so-called Model Production Function, MPF) obtained with three different values of H , which will be used for the age assessment of Rachmaninoff and Raditladi basin. In all cases, the transition in the scaling law is set at $r = H/7.5$. Depending on the relative position of the S-shaped feature with respect to the crater SFD, a maximum age variation of a factor 3-4 can occur.

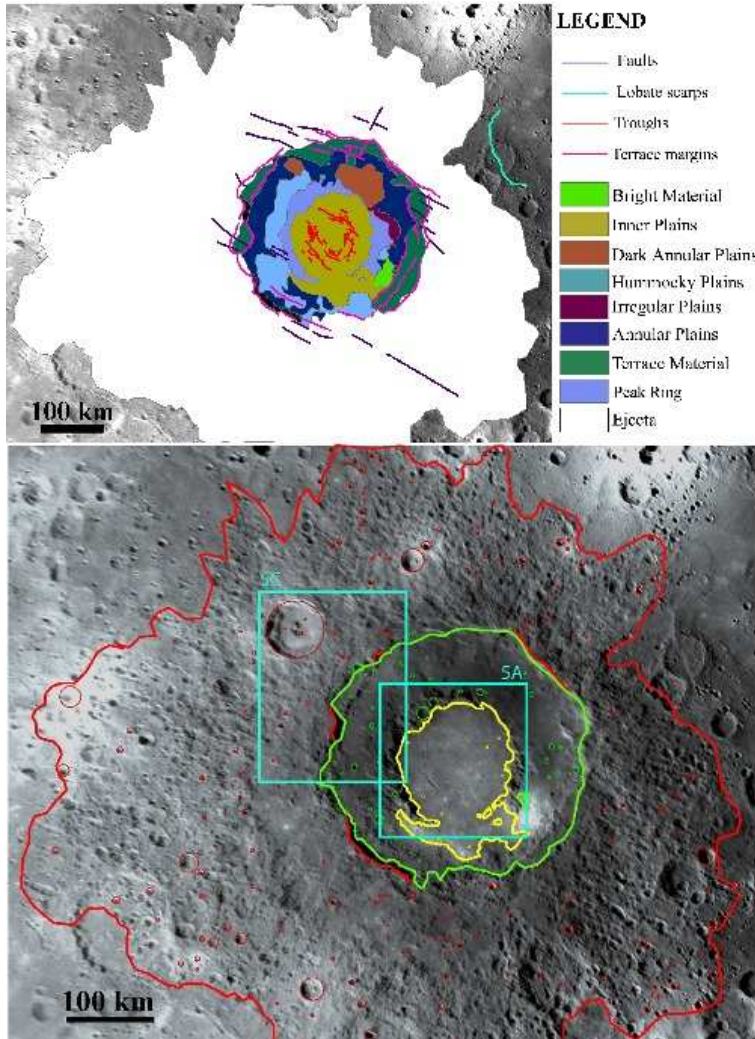


Figure 4: Upper panel: Rachmaninoff geological sketch. Lower panel: Bonafide craters within the three regions considered for crater counts. Boundaries and bonafide craters are in yellow for the inner plains, green for the annular units and red for the ejecta blankets. The counting areas are: 1.74×10^4 , 4.67×10^4 and 3.32×10^5 km² for inner plains, annular units and ejecta blanket, respectively. Boxes indicate close views of fig. 5.

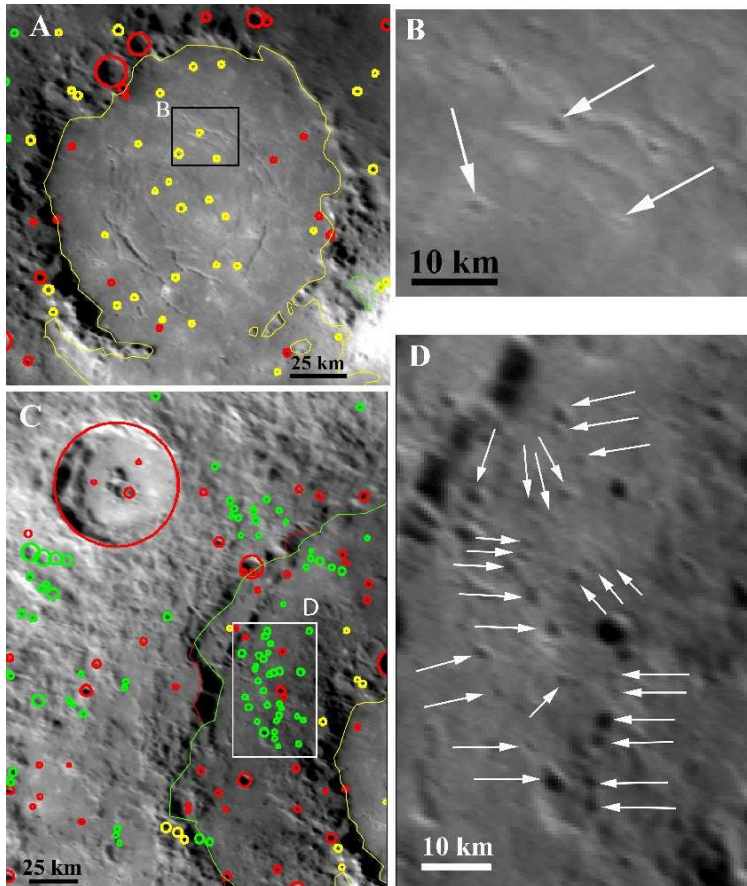


Figure 5: A) Close view of the plains within the Rachmaninoff peak ring: red circles = bonafide craters, yellow circles = circular features of endogenic origin; green circles = secondary craters. B) Detail of endogenic features (white arrows), often with irregular shapes and generally related to troughs and/or surrounded by brighter aloes. C) Close view of a primary peak crater (60 km of diameter) and related secondary craters: red circles = bonafide craters, yellow circles = circular features of endogenic origin; green circles = secondary craters. D) Detail of secondary craters (white arrows) often with elliptical shapes and associated in chains and loops.

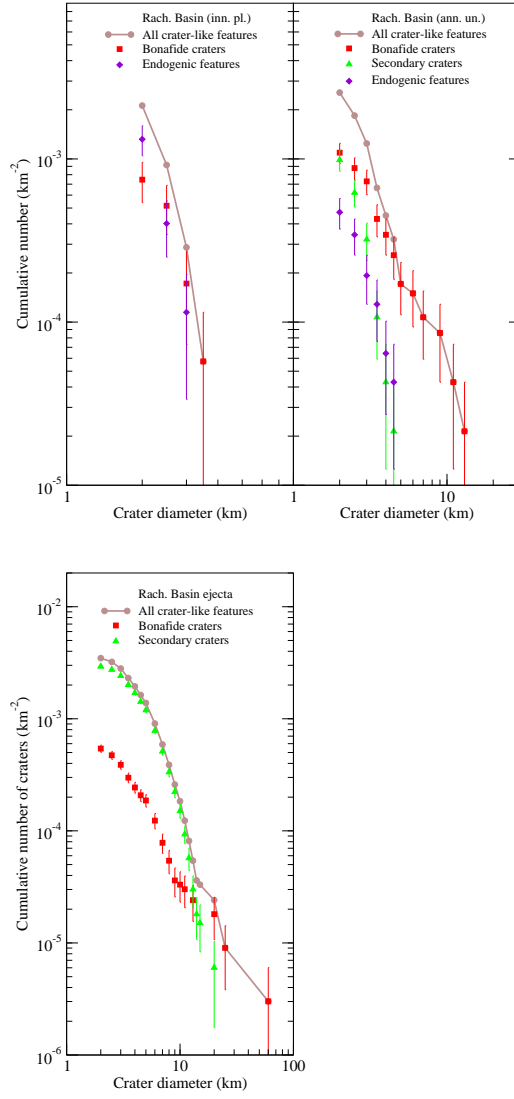


Figure 6: Rachamaninoff basin SFDs of the detected features for inner plains and annular units (upper panels) and ejecta (lower panel).

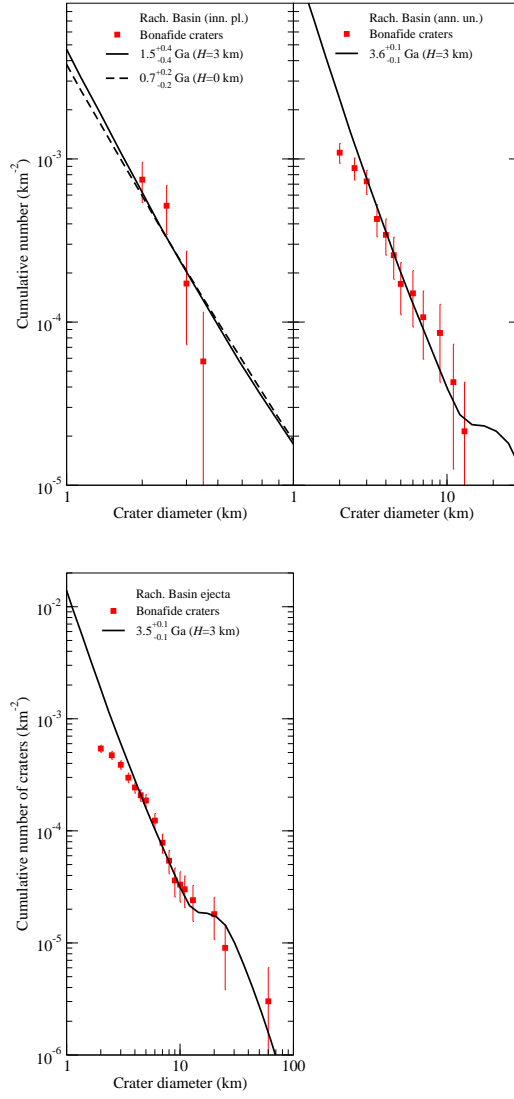


Figure 7: Rachmaninoff age assessment. MPF best fit of the bonafide crater SFDs for the inner plains and annular units (upper panels) and ejecta (lower panel).

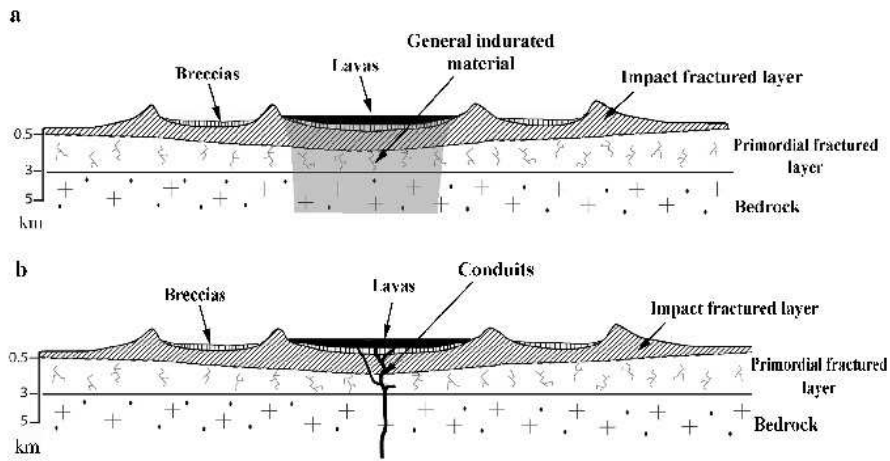


Figure 8: Possible geological sections of the Rachmaninoff basin hypothesized from the fit of MPF with the crater SFD of ejecta, annular materials and inner plains: a) rising magmas and lavas completely hardened the former horizon made up of primordial and impact related fractured material ($H = 0$ km); b) a weakly sustained volcanism emplaced a thin lava layer on top of the fractured material with magma influx concentrated along few conduits ($H = 0.7$ km).

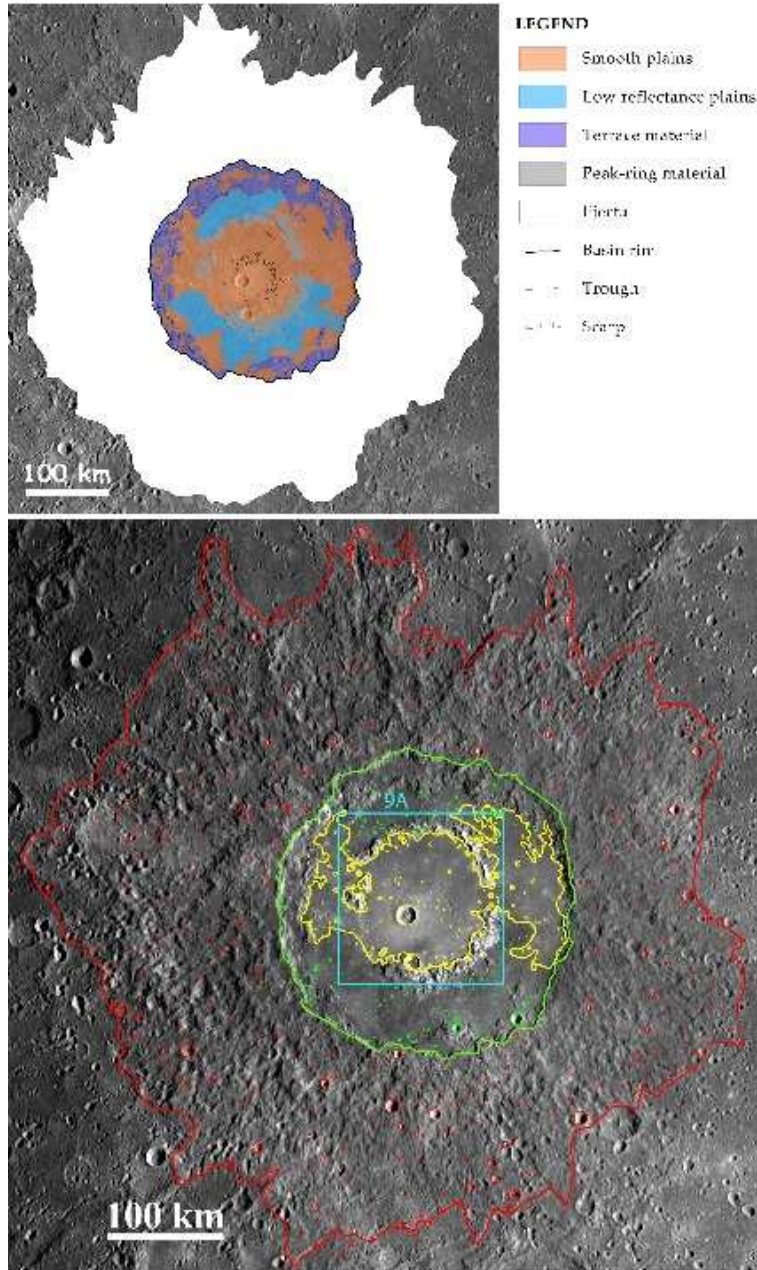


Figure 9: Upper panel: Raditladi geological sketch. Lower panel: Bonafide craters within the three regions (inner plains, annular units, and ejecta blankets) considered for crater counts. Boundaries and bonafide craters are in yellow for the inner plains, green for the annular units and red for the ejecta blankets. The counting areas are: 1.95×10^4 , 3.39×10^4 and $2.01 \times 10^5 \text{ km}^2$ for inner plains, annular units and ejecta blanket, respectively. Boxes indicate close view of fig. 10.

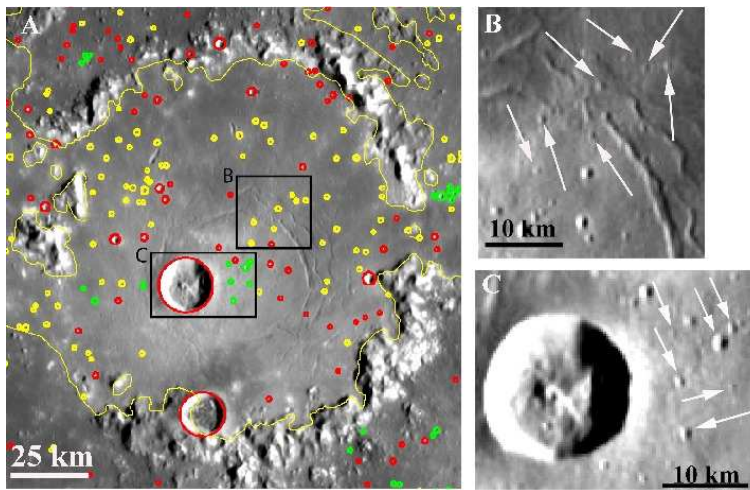


Figure 10: A) Close view of the plains within the Raditladi peak ring: red circles = bonafide craters, yellow circles = circular features of endogenic origin; green circles = secondary craters. B) Detail of endogenic features (white arrows), often with irregular shapes and generally related to troughs and/or surrounded by brighter aloes. D) Close view of a primary peak crater (18 km of diameter) and related secondary craters (white arrows).

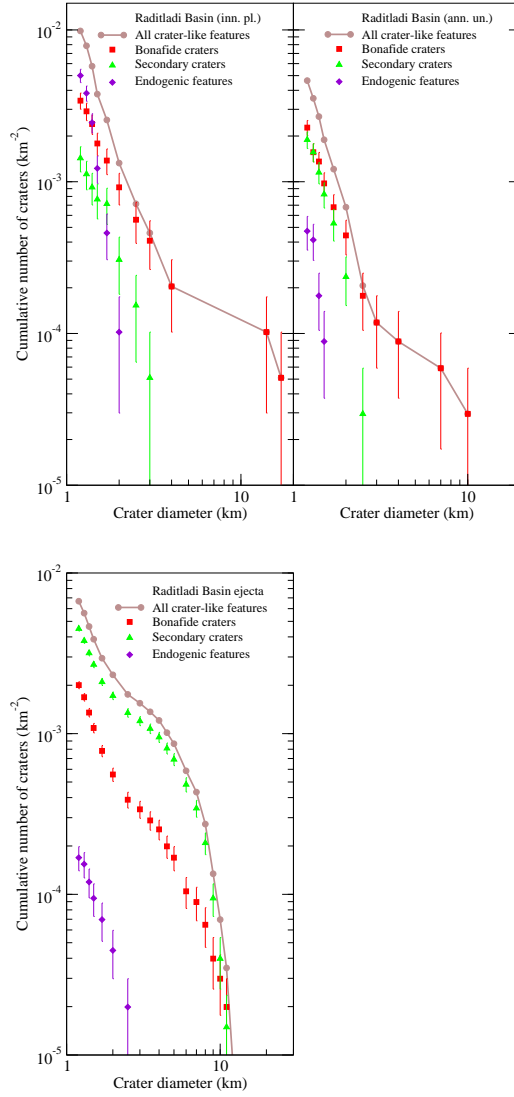


Figure 11: Raditladi basin SFDs of the detected features for inner plains and annular units (upper panels) and ejecta (lower panel).

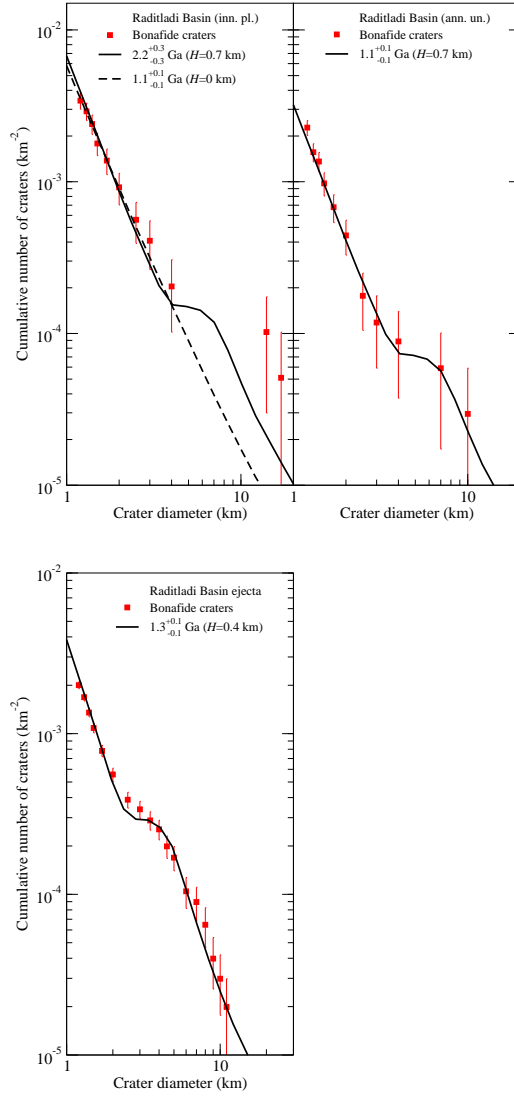


Figure 12: Raditladi age assessment. MPF best fit of the bonafide crater SFDs for the inner plains and annular units (upper panels) and ejecta (lower panel).

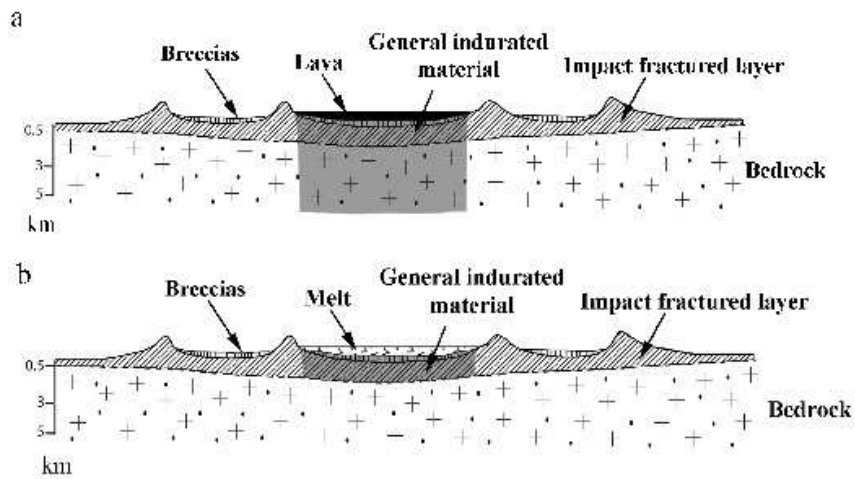


Figure 13: Possible geological sections of Raditladi basin hypothesized from the fit of MPF with the crater SFD of ejecta, annular materials and inner plains. Two scenarios can be argued to justify a very low value of H for the inner plains a) lavas emplaced soon afterward the impact hardened the fractured and brecciated material within the basin or, b) impact melts completely hardened or replaced the impact breccias.